Proceedings of the ASME 2012 Summer Heat Transfer Conference
HT2012
July 8-12, 2012, Rio Grande, Puerto Rico

HT2012-58323

MULTI-SCALE MODELLING OF A SOLAR REACTOR FOR THE HIGH-TEMPERATURE STEP OF A SULFUR-IODINE-BASED WATER SPLITTING CYCLE

Sophia Haussener
Department of Mechanical Engineering, EPFL
1015 Lausanne, Switzerland
and
Environmental Energy Technology Division, LBNL
Berkeley, CA 94720, USA

Dennis Thomey
Institute of Solar Research, DLR
51174 Köln, Germany

Martin Roeb
Institute of Solar Research, DLR
51174 Köln, Germany

Aldo Steinfeld
Department of Mechanical Engineering, ETH
8092 Zürich, Switzerland
and
Solar Technology Laboratory, PSI
5232 Villigen, Switzerland

ABSTRACT

The 3-step sulphur-iodine-based thermochemical cycle for splitting water is considered. The high-temperature step consists of the evaporation, decomposition, and reduction of H_2SO_4 to SO_2 using concentrated solar process heat. This step is followed by the Bunsen reaction and HI decomposition. The solar reactor concepts proposed are based on a shell-and-tube heat exchanger filled with catalytic packed beds and on a porous ceramic foam to directly absorb solar radiation and act as reaction site. The design, modeling, and optimization of the solar reactor using complex porous structures relies on the accurate determination of their effective heat and mass transport properties. Accordingly, a multi-scale approach is applied. Ceramic foam samples are scanned using high-resolution X-ray tomography to obtain their exact 3D geometrical configuration, which in turn is used in direct pore-level simulations for the determination of the morphological and effective heat/mass transport properties. These are incorporated in a volume-averaged (continuum) model of the solar reactor. Model validation is accomplished by comparing numerically simulated and experimentally measured temperatures in a 1 kW reactor prototype tested in a solar furnace. The model is further applied to analyze the influence of foam properties, reactor geometry, and operational conditions on the reactor performance.

1. INTRODUCTION

Thermochemical and hybrid thermo-electrochemical sulfur-based cycles have been proposed as an alternative route for the solar H_2 generation from H_2O at relatively moderate temperatures but at the expense of a corrosive environment. Two sulfur-based water-splitting cycles are introduced: a hybrid (thermochemical/electrochemical) sulfur-based cycle and a 3-step thermochemical sulfur-iodine based cycle. Both cycles include the same high-temperature step described by the net chemical reaction:

$$H_2SO_{4,fl} \rightarrow H_2SO_{4,g} \rightarrow H_2O + SO_3 \rightarrow H_2O + SO_2 + 1/2O_2. \quad (1)$$

Sulfuric acid is evaporated and decomposed at approximately 610 K and the resulting SO_3 is reduced to SO_2 at 1500 K. The temperature of the SO_3 reduction step can be reduced when using catalysts such as Pt, Fe_2O_3, or mixtures of Pt and TiO_2 [23,24]. In the hybrid sulfur-based cycle [25,26], the subsequent step is an electrochemical reaction of water and SO_2, described by:

$$2H_2O + SO_2 \rightarrow H_2SO_4 + H_2. \quad (2)$$

SO_2 is oxidized to H_2SO_4 at the anode ($SO_2 + 2H_2O \rightarrow H_2SO_4 + 2H^- + 2e^-$) and H_2 is formed at the cathode of the electrolyser ($2H^+ + 2e^- \rightarrow H_2$). Sulfuric acid is re-used in the high-

temperature reaction given by eq. (1). The net reaction is $H_2O \rightarrow H_2 + ½ O_2$. The electrolyzer requires less than 15% of the electrical power needed for conventional direct H_2O electrolysis, theoretical 0.17 V in reaction (2) versus theoretical 1.23 V for conventional direct water splitting. In the sulfur-iodine based cycle [27,28,29,30], the Bunsen reaction, described by eq. (3) and taking place at 400 K, follows the high temperature step, resulting in two immiscible aqueous solutions consisting of aqueous sulfuric acid and HI. They are separated and piped to the decomposition reactions (4) and (1). The former takes place at 400 to 600 K.

$$2H_2O + SO_2 + I_2 \rightarrow H_2SO_4 + 2HI. \quad (3)$$

$$2HI \rightarrow I_2 + H_2. \quad (4)$$

The cycles work in a corrosive environment at high temperatures, therefore research has been focused on corrosion and high-temperature resistant materials, as well as membranes for product gas separation. As the temperatures needed are relatively moderate compared to other thermochemical water splitting cycles, the heat source for the high temperature step given by eq. (1) proposed initially was waste heat from nuclear power plants. Recently, solar driven evaporation and decomposition have gained attention. Two exemplary research projects funded by the European Commission are HYTEC [31] and HycycleS [32]. Equilibrium calculations of the reaction are shown in figure 1 for 0.1, 1 and 10 bar. Higher pressure shifts the equilibrium position to the left, due to Le Chatelier's principle. Theoretical maximum energy efficiency of 47% is achieved for the 3-step sulfur-iodine cycle [33].

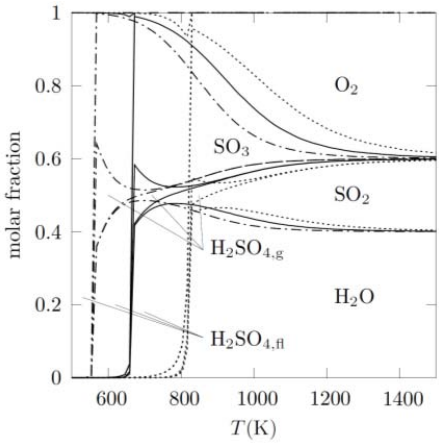

Fig. 1. Equilibrium composition of sulfuric acid evaporation and decomposition at 0.1 bar (dash dotted line), 1 bar (solid line), and 10 bar (dotted line).

Solar reactor concepts for the sulfuric acid evaporation and decomposition are based on honeycombs and RPCs [34], and on shell-and-tube configuration with a packed (catalyst) bed [35]. A two chamber reactor allows for individual evaporation/decomposition and SO_3 reduction reactions [11], as shown in figure 2. The evaporation/decomposition reactor uses RPC as radiation absorber and the SO_3 reduction reactor uses a honeycomb structure. The porous structures provide efficient volumetric absorption of concentrated solar radiation and large specific surface area for evaporation, decomposition and reduction.

Fig. 2. Photo of the two-chamber evaporation/decomposition (left side) and SO_3 reduction reactor (right side).

In this paper, an evaporator/decomposition reactor model is developed following a multi-scale approach: (*i*) at the pore-level scale, where the morphological and heat/mass transfer characterization of the porous absorber is obtained based on the exact morphology obtained by tomography, and (*ii*) at the continuum scale, where the effective transport properties are used in a spatially-averaged reactor model coupling heat and mass transfer with fluid flow and chemistry.

2. PORE-LEVEL SCALE SIMULATIONS

The effective morphological and transport properties of a 20ppi (ppi = pores per inches, d_{nom} = 1.27 mm) SiSiC foam sample, treated by a strut filling technique [1], were investigated in detail elsewhere [2]. A short summary is given below. Computer tomography (CT) in conjunction with Monte Carlo (MC) and finite volume (FV) numerical techniques [2-8] were used to determine its effective morphological and transport properties. A rendered 3D sample of the digitalized foam sample is shown in figure 3.

Porosity, specific surface, pore size distribution and representative elementary volume are tabulated in table 1. The two-point correlation function, calculated by Monte Carlo (MC) sampling and opening operations are used for the determination of the morphological properties.

The effective heat transfer properties, namely extinction coefficient, scattering coefficient, scattering phase function, conductivity, and heat transfer coefficient are listed in table 2. The effective mass transfer properties, namely permeability, Dupuit-Forchheimer coefficient, tortuosity and residence time distributions, and dispersion tensor are shown in table 3.

These effective properties are incorporated in the continuum model. When needed, correlations for their dependency on d_{nom} (e.g. extinction coefficient) are applied.

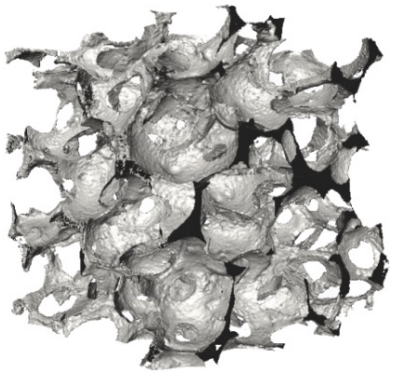

Fig.3. 3D surface rendering of the digitalized geometry of the 20 ppi SiSiC foam.

Table 1. Morphological properties of the 20 ppi SiSiC foam.

Property	Value
Porosity, ε	0.91 (experimental: 0.90±0.02)
Specific surface (m^{-1}), A_0	1680
REV edge length (mm)	4.44
Nominal pore diameter (mm), d_{nom}	1.27
Hydraulic pore diameter (mm)	2.24
Mean pore diameter (mm)	1.55
Median diameter of pores (mm)	1.62
Mode diameter of pores (mm)	1.65

Table 2. Effective heat transfer properties of the 20 ppi SiSiC foam.

Property	Value
Extinction coefficient	431 m^{-1}
Scattering coefficient	43 m^{-1}
Scattering phase function	$0.547\mu_s^2$-$1.388\mu_s$+0.818, with $\mu_s=\cos(\theta_s)$
Conductivity, k, (fluid-to-solid conductivity k_f/k_s) ($Wm^{-1}K^{-1}$)	$k_s\left(0.735\frac{k_f/k_s}{\varepsilon(1-k_f/k_s)+k_f/k_s}+0.267\left(\varepsilon\frac{k_f}{k_s}+1-\varepsilon\right)\right)$
Heat transfer coefficient, h_{sf} ($Wm^{-2}K^{-1}$)	$k_f/d_{nom}(6.820+0.198\cdot Re^{0.788}Pr^{0.606})$

Table.3. Effective mass transfer properties of the 20 ppi SiSiC foam.

Property	Value / formula
Permeability	$5.69\cdot10^{-8}$ m^2
Dupuit-Forchheimer coefficient	519 m^{-1}
Mean tortuosity	1.07
Mean residence time for l_{sample} = 7.6mm (s)	$0.237\cdot Re^{-1.003}$
Perpendicular and parallel component of the dispersion tensor dependent on kinematic viscosity, ν, for Re<5 (m^2/s)	$\nu\cdot6.56\cdot10^{-3}Re$, $\nu\cdot6.30\cdot10^{-1}Re$

3. CONTINUUM-SCALE SIMULATIONS

3.1. Model

The continuum model used to simulate the solar evaporation process in the porous foam is derived by spatially averaging mass, species, momentum and energy equations [9,10]. Averaging models use the intrinsic average, defined as:

$$\langle\psi\rangle^{\alpha}=\frac{1}{V_\alpha}\int_{V_\alpha}\psi\mathrm{dV}\,. \tag{5}$$

It is related to the superficial average by:

$$\langle\psi\rangle=\varepsilon_\alpha\langle\psi\rangle^{\alpha}\,. \tag{6}$$

Additionally, the spatial averaging theorem [9]:

$$\langle\nabla_{\mathbf{r}}\psi\rangle=\nabla_{\mathbf{x}}\langle\psi\rangle+\frac{1}{V}\int_{A_{\text{interface}}}\psi\hat{\mathbf{n}}\mathrm{dA}_{\text{interface}} \tag{7}$$

is applied. The foam absorber in the developed solar evaporator [11] is modeled in a 3D domain, as schematically shown in figure 4. Only the foam, as the relevant part for heat and mass transfer within the reactor, is considered. The governing equations are formulated by spatial averaging of the governing equations in each phase of the foam. The energy equation for the solid phase is given by:

$$\begin{aligned}&\nabla\cdot\left(k_e\nabla\langle T\rangle^s\right)-\nabla\cdot\mathbf{q}_r+\sum_{j,\dot n_j>0}\dot n_j\bar h_{j,\langle T\rangle^s}\\&-\sum_{j,\dot n_j<0}\dot n_j\bar h_{j,\langle T\rangle^f}+\frac{VA_0}{\varepsilon}h_{sf}\left(\langle T\rangle^s-\langle T\rangle^f\right)=0\end{aligned} \tag{8}$$

Mass, species, momentum and energy conservation in the fluid phase are given by:

$$\nabla\cdot\left(\langle\rho\rangle^f\langle\mathbf{u}\rangle\right)=0\,, \tag{9}$$

$$\nabla\cdot\left(\langle\mathbf{u}\rangle\langle\rho_j\rangle^f\right)-\nabla\cdot\left(\mathbf{D}\cdot\nabla\left(\frac{\langle\rho_j\rangle^f}{\langle\rho\rangle^f}\right)\right)=0\,, \tag{10}$$

$$\begin{aligned}\nabla\left(\langle\rho\rangle^f\langle\mathbf{u}\rangle\langle\mathbf{u}\rangle\right)=&-\nabla\langle p\rangle^f+\nabla\left(\mu_f\nabla\langle\mathbf{u}\rangle\right)-\frac{\mu_f}{K}\langle\mathbf{u}\rangle\\&-F\langle\rho\rangle^f\left|\langle\mathbf{u}\rangle\right|\langle\mathbf{u}\rangle\end{aligned}\,, \tag{11}$$

$$\begin{aligned}\nabla\left(\langle\rho\rangle^f\langle\mathbf{u}\rangle h\right)=&-\nabla\cdot\left(k_f\nabla\langle T\rangle^f\right)-\sum_{j,\dot n_j>0}\dot n_j\left(\bar h_{j,\langle T\rangle^s}-\bar h_{j,\langle T\rangle^f}\right)\\&+\frac{VA_0}{\varepsilon}h_{sf}\left(\langle T\rangle^s-\langle T\rangle^f\right)\end{aligned}\,. \tag{12}$$

The morphological and effective transport parameters (such as ε, A_0, k_e, h_{sf}, K, F, …) in Eqs. (8)-(12) were determined in the previous characterization study [2] and can be readily plugged in. The equations are solved with a commercial CFD code [12] using a dual cell approach [13].

The front of the reactor's foam (corresponding to the inlet of the carrier gas and the solar radiation) is described by the xy-plane at z = 0.04 m, while the outlet of the product gases is described by the xy-plane at z = 0 m. Tubes deliver the sulfuric acid to the foam center (approximately at z = 0.02 m), in counterflow to the carrier gas.

a)

b)

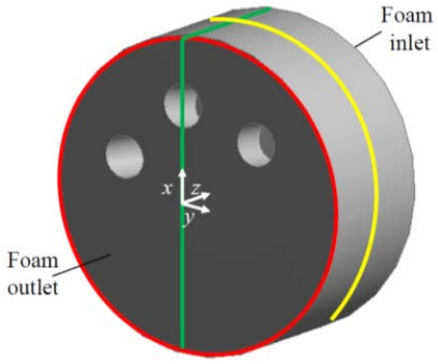

Fig.4. (a) Front view of solar evaporator reactor containing the foam. The insulation has been removed. (b) Back view of foam's model domain used for the numerical calculations. The foam inlet (where carrier gas and solar radiation enters), foam outlet (marked by red boundary) and cut planes used later (marked by green and yellow boundaries) are shown. The three holes mark the inlet tubes for delivering sulfuric acid, in counterflow to the carrier gas.

3.2. Boundary conditions

The boundary conditions applied to Eqs. (8)-(12) are:

at the acid inlet:

$$\bar{\mathbf{u}}\cdot\hat{\mathbf{n}} = -u_{\text{acid,in}},\ T_f = T_{\text{acid,in}},\ x_{\text{acid}} = 1, \tag{13}$$

at the front:

$$\bar{\mathbf{u}}\cdot\hat{\mathbf{n}} = -u_{\text{carrier,in}},\ T_f = T_{\text{carrier,in}},\ x_{\text{acid}} = 0,\ \mathbf{q}''\cdot\hat{\mathbf{n}} = -q''_{\text{rad,in}}, \tag{14}$$

at the outlet:

$$p = p_{\text{atm}}, \tag{15}$$

at the lateral wall:

$$\bar{\mathbf{u}}\cdot\hat{\mathbf{n}} = 0,\ \hat{\mathbf{n}}\cdot\nabla\bar{\mathbf{u}} = 0,\ \mathbf{q}''\cdot\hat{\mathbf{n}} = q''_{nc} + q''_{cond}\,. \tag{16}$$

$T_{\text{acid,in}}$ and $u_{\text{acid,in}}$ (velocity magnitude normal to the boundary) are given at the sulfuric acid inlet, given by the three tubes entering the foam. The carrier gas used to clean and cool the window is assumed to enter from the front (xy-plane at z = 0.04 m) perpendicular to the reactor axis and with uniform $u_{\text{carrier,in}}$ and $T_{\text{carrier,in}}$, described by Eq. (13). The initial solid temperature is chosen equal to $T_{\text{carrier,in}}$. No slip boundaries are assumed at the lateral reactor walls. The heat flux boundary through the lateral walls, Eq. (16), accounts for conduction losses (insulation composed of Al_2O_3 and SiO_2, k = 0.11 W/(mK) at 623 K, given by the manufacturer) and natural convection losses at the outer reactor wall. The latter are described by Eq. (17) [14]. Both losses are incorporated into a combined heat transfer coefficient, which is calculated to be 3 W/(m^{2}K).

$$\text{Nu} = \left[0.60 + \frac{0.387\text{Ra}^{1/6}}{\left(1+\left(0.559/\text{Pr}\right)^{9/16}\right)^{8/27}}\right] \tag{17}$$

For simplification, the reactor walls are assumed to be perfect diffuse reflectors, as justified by the high reflectance values of alumina [15]. The solar radiation entering through the aperture is given by its flux, $q_{\text{rad,in}}$". The spatial solar flux distribution is obtained by fitting a Gaussian distribution to the experimentally measured flux distributions at the aperture, shown in figure 5. The directional distribution of the incident solar radiation can be approximated by a cone shaped distribution, as supported by modeling and measurements [16,17]. For the DLR's solar furnace, the directional distribution is assumed to be uniform in a cone with half opening angle of 25°. The incident solar flux is reduced by 8% to account for the window transmittance in the wavelength region of interest, described by Eqs. (18)-(20).

$$Tr_{\lambda,\theta} = \tau_{\lambda,\theta}\frac{1-r_{\lambda,\theta}}{1+r_{\lambda,\theta}}\frac{1-r_{\lambda,\theta}^{\,2}}{1-r_{\lambda,\theta}^{\,2}\tau_{\lambda,\theta}^{\,2}} \tag{18}$$

$$r_{\lambda,\theta} = 0.5\frac{\sin^2(\theta-\chi)}{\sin^2(\theta+\chi)}\left(1+\frac{\cos^2(\theta+\chi)}{\cos^2(\theta-\chi)}\right),\quad \text{with}\ \frac{\sin\chi}{\sin\theta} = \frac{n_{1,\lambda}}{n_{2,\lambda}} \tag{19}$$

$$\tau_{\lambda,\theta} = \exp\left(-\kappa_\lambda\frac{l_{\text{sample}}}{\cos\chi}\right) \tag{20}$$

The transmitted fraction, Tr, is calculated by the reflectance, r, and transmittance, τ, of the window. Each of them is a function of the wavelength of the incident radiation, λ, and the refractive index of air and glass, n_1 and n_2, respectively. θ and χ describe

the inlet and outlet angle of the ray with respect to the surface normal vector.

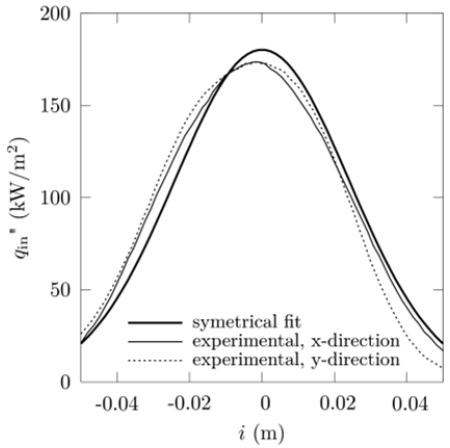

Fig.5. Measured spatial solar flux distribution and Gaussian fit for measurements with a target of 0.04 m^2 and 0.55 kW total power input (RMS=5.4).

The H_2SO_4 inlet flow is diluted with 50 wt% H_2O. The diluted acid properties are calculated by mass-weighted summation of the specific properties. It is assumed that the inlet liquid flow is instantaneously evaporated and, therefore, a two-phase medium model is applied, i.e. only the vapour phases of H_2SO_4 and H_2O and the solid foam are considered. Correspondingly, compression effects due to evaporation-related density changes are neglected in the simulation domain considered. The evaporation is modelled by a heat sink:

$$\begin{aligned} Q_{\text{sink,evap}} = &(h_{\text{H}_2\text{SO}_4,T_{\text{evap}}} - h_{\text{H}_2\text{SO}_4,T_{\text{in}}})x_{\text{H}_2\text{SO}_4}\dot{m}_{\text{H}_2\text{SO}_4} \\ &+ \dot{m}_{\text{H}_2\text{SO}_4}x_{\text{H}_2\text{SO}_4}\Delta h_{\text{evap,H}_2\text{SO}_4} \\ &+ (h_{\text{H}_2\text{O},T_{\text{evap}}} - h_{\text{H}_2\text{O},T_{\text{in}}})\left(1-x_{\text{H}_2\text{SO}_4}\right)\dot{m}_{\text{H}_2\text{O}} \\ &+ \dot{m}_{\text{H}_2\text{O}}\left(1-x_{\text{H}_2\text{O}}\right)\Delta h_{\text{evap,H}_2\text{O}} \end{aligned} \quad (21)$$

which accounts for the sensible heat and the evaporation enthalpy. Dissociation enthalpy of the acid is neglected in this first modeling approach.

3.3. Continuum results

3.3.1. Comparison to experiments

Temperature measurements from experimental campaigns performed at DLR's solar furnace [18] are used to validate the model and to estimate its accuracy. A 90 mm-diameter 40 mm-thickness foam was used. Thermocouples (type K) have been inserted into the foam from the back of the reactor to estimate an average temperature. Figure 6a shows a cutting plane through the foam center (z = 0.02 m, yellow plane indicated in figure 4b) indicating the position of the thermocouples used for the temperature measurements, T_1-T_6. Thermocouple T_7 is located at the outlet. Measured temperatures, power input, and acid inflow are shown in figure 6b. The temperature and power input measurements are averaged over each run – beginning with the start of the acid inflow and ending with the stop of the acid inflow – resulting in an averaged, steady state temperature and an averaged power input, and corresponding standard deviations. Figure 7 compares the measured (averages and standard deviations) and the simulated temperatures for the experimental run, described in Table 4.

The discrepancies observed between the experimentally determined and numerically calculated temperatures at positions 4 and 6 are associated to asymmetric angular distribution of the incident radiation. The difference observed at position 5 is associated to degradation in the insulating material and, consequently, higher heat losses in the experiment than modeled.

a)

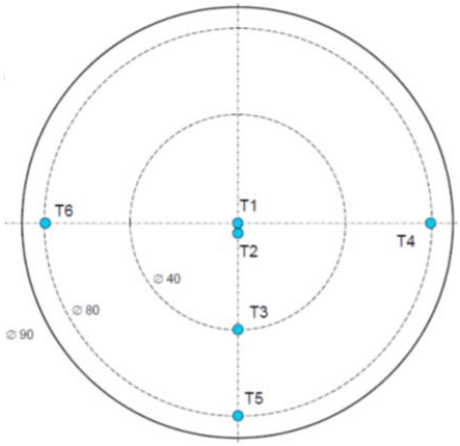

b)

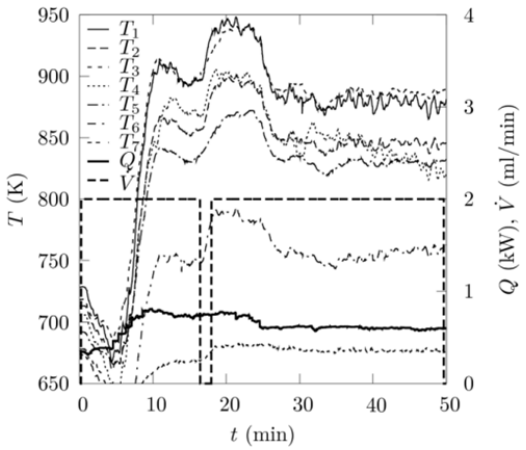

Fig. 6. Cutting plane through the foam center (see yellow plane indicated in figure 4b) indicating the location of the thermocouples used for the temperature measurements (a). Recorded temperatures (left axis), and power input and volumetric flow rate of acid inflow (right axis) of the solar experimental run.

Table 4. Experimental conditions: acid inflow, carrier gas inflow and solar power input.

	Acid inlet (ml/min)	Carrier gas inlet (cm^3/min)	Solar power input (kW)
experiment	2	0.259	0.629

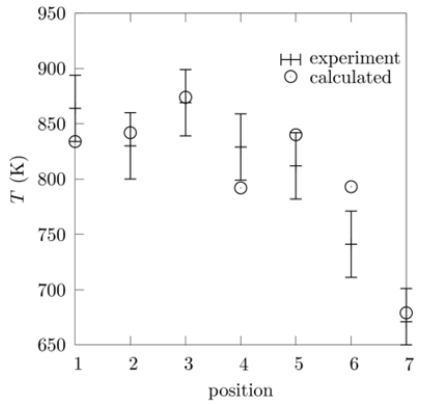

Fig. 7. Comparison of experimentally obtained (averaged over experimental duration) and the numerically determined temperatures at the positions indicated in figure 6a.

3.3.2. Reference case

The previously described case serves as the reference (baseline) case for the following parameter study. The conditions of the reference case are given by a total inflow of 2 ml/min diluted sulfuric acid (50 wt% H_2SO_4, 50 wt% H_2O), a solar power input of 0.629 kW and a carrier gas inflow of 0.259 cm^3/min.

The temperature distributions in the *xz*-plane (through the center inlet tube, at $y = 0$, green plane indicated in figure 4b) for the two phases are shown in figure 8. The carrier gas flowing in from the front ($z = 0.04$ m) at 300 K reaches the solid temperature within less the 5 mm. The temperature of a small fraction of the fluid phase at the acid inlet bellow the evaporation temperature of the acid indicates that the acid needs a finite amount of time to reach a hot surface and to be evaporated.

a)

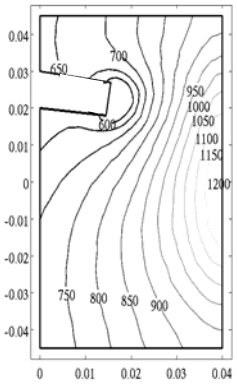

b)

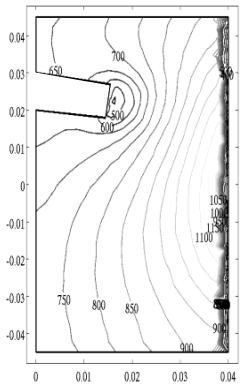

Fig. 8. Temperature distribution in solid (a) and fluid (b) phase in cutting *xz*-plane, green plane indicated in figure 4b, through center of inlet tube (partially visible).

The temperature distributions at the reactor's foam outlet (red plane indicated in figure 4b) are shown in figure 9 for the solid and the fluid phase. The lower temperatures at the top of the foam are explained by the position of the acid inlets. The solid temperatures are slightly lower due to the energy needed for the evaporation, solely delivered by the solid matrix. The stream lines and their velocity magnitude are shown in figure 10, indicating the change in direction and the decrease in velocity due to the porous foam and the carrier gas in counterflow. The calculated solid to fluid volumetric heat transfer shows that at the carrier gas inlet ($z = 0.04$ m) heat is transferred from the solid matrix, heated by the solar irradiation, to the fluid. At the acid inlet (approximately $z = 0.02$ m) the solid matrix is rapidly cooled due to the instantaneous evaporation of the acid. Heat is transferred from the hot carrier gas and the hot acid to the solid matrix. At the outlet the solid matrix ($z = 0$ m) and the fluid are nearly at the same temperature, still a small portion of heat is transferred from the heated fluid phase to the solid phase.

a)

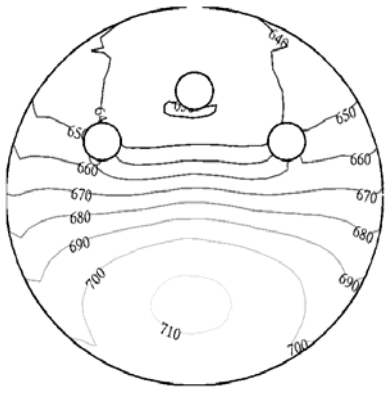

b)

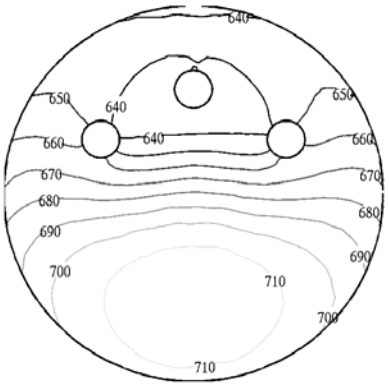

Fig. 9. Temperature distribution at the foam outlet (see red plane in figure 4b) for the solid phase (a) and for the fluid phase (b). The three holes indicate the tubes by which the acid is delivered into the foam center.

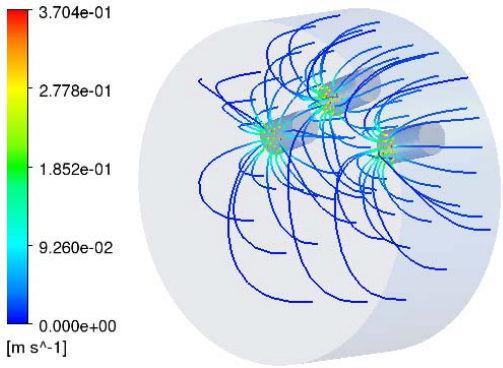

Fig. 10. Front view of the foam showing stream lines starting at the acid inlets, where acid flows in in counterflow to the carrier gas. The color indicates the velocity magnitude in m/s.

3.3.3. Parameter study

Two efficiencies are defined. The energetic efficiency is based on the energy used to heat reactants and carrier gas and for the phase change:

$$\eta_{\text{en}} = \frac{\sum_{n_s} x_i \dot{m}_i h_{i,T_o} - \sum_{n_s} x_i \dot{m}_i h_{i,T_{\text{in}}}}{A_{\text{in}} q''_{\text{in}}} \qquad (22)$$

The chemical efficiency is defined based on the energy used solely for evaporation:

$$\eta_{\text{chem}} = \frac{\dot{m}_{\text{acid}} \Delta H_{\text{evap}}}{A_{\text{in}} q''_{\text{in}}} \qquad (23)$$

Reaction conversion, X_{evap}, is defined as the fraction of evaporated acid-water solution (temperatures > T_{evap} = 548 K) to the total inlet acid-water solution. Based on the reference case (q_{in} = 0.629 kW, $\dot{m}_{\text{acid}}$ = 2 ml/min, d_{nom} = 1.27 mm, d_{tubes} = 9 mm, n_{tubes} = 3, l_{foam} = 40 mm), the operational conditions (acid inflow and solar irradiation), and geometrical properties (acid inflow tube diameter, foam thickness, nominal pore diameter) are varied while all other parameters are kept constant. Variation in operational conditions and their influence on the reactor performance are shown in figure 11. Decreasing the inlet radiative flux leads to lower temperatures in the foam but to higher efficiencies due to lower re-radiation losses. Radiative inlet power below 600 W doesn't allow for a complete evaporation. As expected, increasing the acid inflow leads to a decrease in temperature. At high mass flow rates, the lower temperatures result in limited reaction conversion, which in turn lead to a reduction in efficiencies.

a)

b)

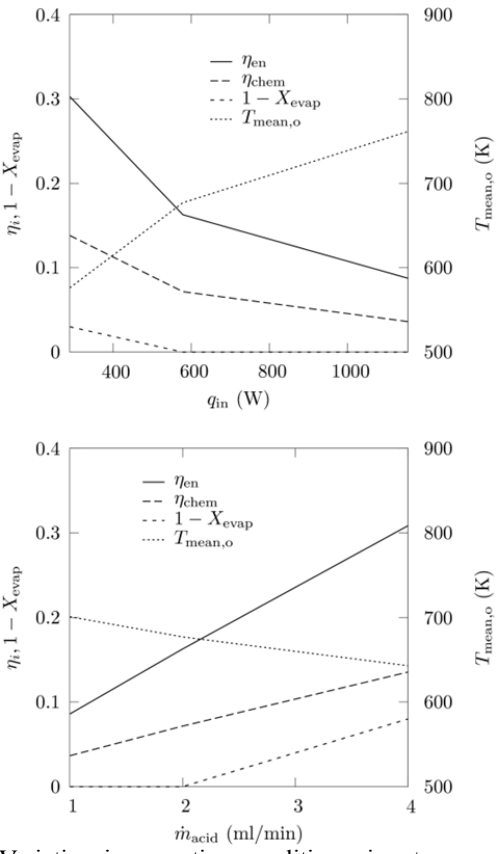

Fig.11. Variation in operating conditions, input power (a) and inlet acid flow (b), and their influence on reactor's energetic and chemical efficiency and mean outlet temperature.

Changing the nominal pore diameter in a range typically available (10, 20 and 40 ppi corresponding to 2.53, 1.27 and 0.635 mm d_{nom}) while assuming that there are no significant changes in pore size distribution (morphology) and porosity has several effects on the transport properties of the foam. Increasing the pore size decreases the absorption of the foam [19,20], allowing the radiation to penetrate deeper into the foam and heating it more uniformly.

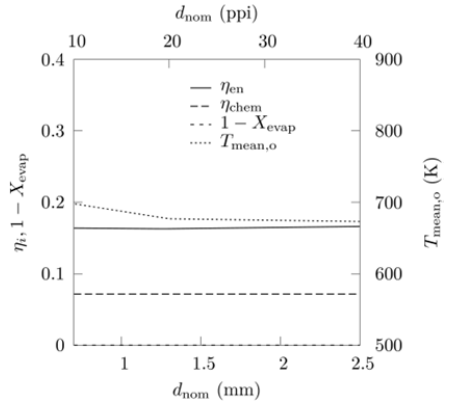

Fig.12. Influence of changes in the foams pore size on the reactor's energetic and chemical efficiency and mean outlet temperature.

a)

b)

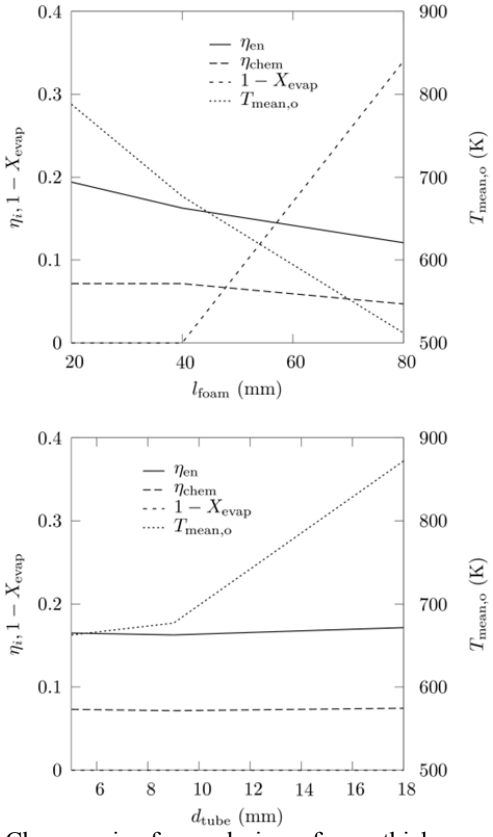

Fig.13. Changes in foam design, foam thickness (a) and diameter of inlet tubes (b), and their influence on reactor's energetic and chemical efficiency and mean outlet temperature.

A small increase in energetic efficiency is observed while the chemical efficiency stays constant due to the fact that all the incoming acid evaporates for all pore sizes analyzed, see figure 12. Decreasing the pore size decreases permeability, and consequently increases the pressure drop in the foam, and increases Dupuit-Forchheimer coefficient [8,21,22]. This leads to an increase in residence time and tourtosity which allows heating up the fluid to higher temperatures. Increasing pore size leads to higher Nu numbers (see Table 2), allowing for a more efficient convective heat transfer. Nevertheless, these two processes are not dominant. Changes in pore size (at constant porosity and unchanged morphology) do not affect the effective conductivity of the foam [2].

Variations in foam design and their influence on the reactor's performance are shown in figure 13. Decreasing the foam thickness leads to an increase in reactor performance due to the higher temperature reached in the foam. Increasing the diameter of the acid inlet tubes leads also to an increase in reactor performance and mean outlet temperature due to the fact that, with a constant inflow, the acid enters with reduced inlet velocity allowing for a more efficient heat transfer.

4. CONCLUSIONS

A 3D continuum heat/mass transfer model was developed for simulating the solar reactor for performing the high-temperature step of the S-I cycle. The effective transport properties of porous ceramic foam, determined by tomography-based direct-pore level simulations, were incorporated in the model. The effect of varying the foam properties, reactor geometry, and operational condition on the reactor's performance were analyzed. Decreasing the radiative input power and increasing the mass inflow led to increased reactor efficiency, but this trend reversed once the reduced temperatures did not allow for acid evaporation. Decreasing the foam thickness led to a superior reactor performance. Higher mean outlet temperatures were obtained for larger tube diameter of the acid inlet. This reduces the energy needed for the complete sulfur trioxide decomposition. The variation in the foam properties, e.g. variation in the nominal pore diameter at constant porosity and foam morphology, showed no significant effect on reactor efficiencies. The model can serve as a tool for reactor and process optimization.

ACKNOWLEDGMENTS

This work has been financially supported by the European Commission under Contract No. 212470 Project HYCYCLES.

REFERENCES

[1] Adler, J., Teichgraber, M., and Standke, G., "Offenzellige Schaumkeramik mit hoher Festigkeit und Verfahren zu deren Herstellung", DE 196 21 638.9, 30.05.1996.

[2] Haussener, S., Coray, P., Lipiński, W., Wyss, P., and Steinfeld, A., 2010, Tomography-based heat and mass transfer characterization of reticulate porous ceramics for high-temperature processing, *ASME Journal of Heat Transfer,* **132**, 023305.

[3] Petrasch, J., Wyss, P., Stämpfli, R., and Steinfeld, A., 2008, "Tomography-based multiscale analyses of the 3D geometrical morphology of reticulated porous

ceramics", Journal of the American Ceramic Society, **91**, pp. 2659–2665.

[4] Haussener, S., Lipiński, W., Petrasch, J., Wyss, P., and Steinfeld, A., **"**Tomographic Characterization of a Semitransparent-Particle Packed Bed and Determination of its Thermal Radiative Properties", Journal of Heat Transfer, **131**, 072701, 2009.

[5] Petrasch, J., Wyss, P., and Steinfeld, A., "Tomography-based Monte Carlo determination of radiative properties of reticulate porous ceramics", Journal of Quantitative Spectroscopy and Radiative Transfer, **105**, pp. 180–197, 2007.

[6] Petrasch, J., Schrader, B., Wyss, P., and Steinfeld, A., "Tomography-based determination of the effective thermal conductivity of reticulate porous ceramics", Journal of Heat Transfer, 103, pp. 032602/1–10, 2008.

[7] Petrasch, J., Meier, F., Friess, H., and Steinfeld, A., "Tomography based determination of permeability, Dupuit-Forchheimer coefficient, and interfacial heat transfer coefficient in reticulate porous ceramics", International Journal of Heat and Fluid Flow, **29**, pp. 315–326, 2008.

[8] Haussener, S., Lipiński, W., Wyss, P., and Steinfeld, A., **"**Tomography-Based Analysis of Radiative Transfer in Reacting Packed Beds Undergoing a Solid-Gas Thermochemical Transformation", Journal of Heat Transfer, in press.

[9] Whitaker, S., The Method of Volume Averaging. In J. Bear, editor, *Theory and Applications of Transport in Porous Media*, Volume 13. Kluwer Academic Publishers, 1999.

[10] Lipiński, W., Petrasch, J., and Haussener, S., "Application of the spatial averaging theorem to radiative heat transfer in two-phase media", Journal of Quantitative Spectroscopy and Radiative Transfer, **111**, p. 253–258, 2009.

[11] D. Thomey, M. Roeb, P. Rietbrock, J. Säck, C. Sattler, S. Haussener, A. Steinfeld, I. Cañadas, and S. Martínez, "Development of a two-chamber receiver-reactor for the solar decomposition of sulphuric acid", *Proceedings of SolarPACES 2009 Conference*, Berlin 15–18 September 2009.

[12] Ansys Inc., 2009. ANSYS-CFX, www.ansys.com.

[13] Liu, B., Hayes, R., Yi, Y., Mmbaga, J., Checkel, M., and Zheng, M., "Three Dimensional Modelling if Methane Ignition in a Reverse Flow Catalytic Converter", Computers and Chemical Engineering, **31**, pp. 292**–**306, 2007.

[14] Incropera, F., and DeWitt, D., *Introduction to Heat Transfer*. John Wiley & Sons, Inc., New York, 1996.

[15] Tolukian, Y., *Thermophysical Properties of Matter*, Plenum, New York, 1970.

[16] Z'Graggen, A., *Solar gasification of carbonaceous materials – reactor design, modelling and experimentation*, PhD thesis, ETH Zurich, 2008.

[17] Kuhn, P., and Hunt, A., 1991, "A new solar simulator to study high temperature solid-state reactions with highly concentrated radiation", Solar Energy Materials, **24**, pp. 742**–**750.

[18] Neumann, A., and Groer, U., "Experimenting with Concentrated Sunlight Using the DLR Solar Furnace", Solar Energy, **58**, pp. 181**–**190, 1996.

[19] Hendricks, T., and Howell, J, "Absorption/scattering coefficient and scattering phase function in reticulated porous ceramis", Journal of Heat Transfer, **118**, pp. 79**–**87, 1996.

[20] Petrasch, J., *Multi-Scale Analysis of Reactive Flow in Porous Media*, PhD thesis, ETH Zurich, 2007.

[21] Kaviany, M., 1995, *Principles of Heat Transfer in Porous Media*, Springer-Verlag, New York, Berlin, Heidelberg.

[22] Dullien, F., 1979, *Porous Media Fluid Transport and Pore Structure*, Academic Press, New York.

[23] D. Ginosar, L. Petkovic, A. Glenn, and K. Burch. Stability of supported platinum sulfuric acid decomposition catalysts for use in thermochemical water splitting cycles. International Journal of Hydrogen Energy, 32:482–488, 2006.

[24] A. Noglik, M. Roeb, T. Rzepczyk, J. Hinkley, C. Sattler, and R. Pitz-Paal. Solar thermochemical generation of hydrogen: Development of a receiver reactor for the decomposition of sulfuric acid. Journal of Solar Energy Engineering, 131:011003, 2009.

[25] L. Brecher, S. Spewock, and C. Warde. The Westinghouse sulfur cycle for the thermochemical decomposition of water. International Journal of Hydrogen Energy, 2:7–15, 1977.

[26] L. Brecher and C. Wu. Electrolytic decomposition of water. U.S. Patent, no. 3888750, 1975.

[27] J. Norman, G. Besenbruch, L. Brown, D. O'Keefe, and C. Allen. Thermochemical water-splitting cycle, bench scale investigations, and process engineering. Final report for the period February 1977 through December 1981, 1982.

[28] D. O'Keefe, C. Allen, G. Besenbruch, L. Brown, J. Norman, R. Sharp, and K. McCorkle. Preliminary results from bench-scale testing of a sulfuriodine thermochemical water-splitting cycle. International Journal of Hydrogen Energy, 5:831–892, 1982.

[29] X. Vitart, A. Le Duigou, and P. Carles. Hydrogen production using the sulfur-iodine cycle coupled to a

VHTR: An overview. Energy Conversion and Management, 47:2740–2747, 2006.

[30] R. Jones and G. Thomas. Materials for the hydrogen economy. Taylor and Francis Group, Boca Raton, 2008.

[31] A. Le Duigou, J.-M. Borgard, B. Larousse, D. Doizi, R. Allen, B. Ewan, G. Priestman, R. Elder, R. Devonshire, V. Ramos, G. Cerri, C. Salvini, A. Giovannelli, G. De Maria, C. Corgnale, S. Brutti, M. Roeb, A. Noglik, P.-M. Rietbrock, S. Mohr, L. de Oliveira nad N. Monnerie, M. Schmitz, C. Sattler, A. Martinez, D. de Lorenzo Manzano, J. Rojas, S. Dechelotte, and O. Baudouin. Hytec: An EC funded search for a long term massive hydrogen production route using solar and nuclear technologies. International Journal of Hydrogen Energy, 32:1516–1529, 2007.

[32] M. Roeb, D. Thomey, D. Graf, C. Sattler, S. Poitou, F. Pra, P. Tochon, C. Mansilla, J.-C. Robin, F. Le Naour, R. Allen, R. Elder, I. Atkin, G. Karagiannakis, C. Agrafiotis, A. Konstandopoulos, M. Musella, P. Haehner, A. Giaconia, S. Sau, P. Tarquini, S. Haussener, A. Steinfeld, S. Martinez, I. Canadas, A. Orden, M. Ferrato, J. Hinkley, E. Lahoda, and B. Wong. Hycycles – A project on nuclear and solar hydrogen production by sulphur based thermochemical cycles. International Journal of Nuclear Hydrogen Production and Application, 1:1–11, 2010.

[33] C. Bilgen and E. Bilgen. An assessment on hydrogen production using central receiver solar systems. International Journal of Hydrogen Energy, 9:197–204, 1984.

[34] A. Noglik, M. Roeb, T. Rzepczyk, J. Hinkley, C. Sattler, and R. Pitz-Paal. Solar thermochemical generation of hydrogen: Development of a receiver reactor for the decomposition of sulfuric acid. Journal of Solar Energy Engineering, 131:011003, 2009.

[35] S. Lin and R. Flaherty. Design studies of the sulfur trioxide decomposition reactor for the sulfur cycle hydrogen production process. International Journal of Hydrogen Energy, 8:589–596, 1983.